

X-RAY TOMOGRAPHIC CHARACTERIZATION OF IMPURITIES IN POLYCRYSTALLINE ICE

M. M. Miedaner¹, T. Huthwelker², F. Enzmann¹, M. Kersten¹, M. Stampanoni³,
M. Ammann²

¹Environmental Geochemistry, Institute of Geosciences Johannes Gutenberg University,
Becher-Weg 21, D-55099 Mainz, Germany

²Radio and Environmental Chemistry, Paul Scherrer Institute, CH-5232 Villigen,
Switzerland

³Swiss Light Source, Paul Scherrer Institute, CH-5232 Villigen, Switzerland

1 INTRODUCTION

Natural ice may grow by vapor deposition, as it is the case for snowflakes. Additionally, ice also grows from the liquid phase. Examples are droplets in tropospheric clouds, which often consist of dilute solutions of acids and salts (e.g. sulfur dioxide, ammonium sulfate, typically at a 10^{-4} M concentration) and also organic acids¹. Furthermore, ice also forms in brines of higher concentration, such as Sea water (3.5 wt.% NaCl)², or in stratospheric aerosols, which consist of highly concentrated solutions (several 10 wt.%) of various inorganic acids³⁻⁶. When ice forms in such aqueous environments, most impurities are expelled from the crystalline matrix. Hence, multiphase systems are created, which consist of ice, solid salts, gaseous inclusions like air bubbles and highly concentrated inorganic as well as organic solutions.

Ice and its surface host various chemical reactions in nature. Examples include the stratospheric and marine ozone chemistry²⁻⁴. Such reactions may be located on the ice surface itself, or in the inclusions, which provide a strong ionic environment^{7,8}. Hence, to assess the chemical activity of such multiphase systems, it is of interest to study its morphology. Moreover, as micro phases may manifest as a three dimensional network in the ice, it has been predicted theoretically that such structures can play a crucial role for transport processes in ice, even in very clean system, such as ice cores⁹.

However, little is known about the morphology of such multiphase-systems. Morphological studies on impurities in ice are rare, and most of them are based on 2D- rather than 3D-information. Optical^{10,11} and electron microscopy¹²⁻¹⁴, as well as electron micro probe¹⁵ or Raman spectroscopy^{16,17} were used to localize impurities in triple junctions, air bubbles, vapor-deposited ice films, and in slices cut from ice cores. However, 2D-scans cannot provide information on higher-order geometrical attributes such as the connectivity of the impurities in veins. X-ray micro-tomography (XMT) overcomes this imaging problem by providing non-destructive cross-sectional as well as three-dimensional object representations from X-ray attenuation mapping. XMT is increasingly used in glaciology to characterize heterogeneous structural features of intact ice samples at a high spatial resolution. Schneebeli and Sokratov¹⁸ performed XMT using a bench-top device with a resolution of about 15-30 μm located in a cold room to elucidate the morphology of snow. Also a cryo-stage for synchrotron XMT was developed by Brzoska and Flin¹⁹⁻²¹

which provided a 5 μm resolution. However, a voxel of 1 μm^3 is required to detect inclusions in ice via micro-tomography²².

This contribution presents images recorded with a novel setup for synchrotron-based XMT. We investigate multiphase systems consisting of typical aerosol constituents, such as mineral dusts and organic components such as octanol, both pure and mixed with a dilute NaBr solution. To gain inclusions of a size suitable to be detected at the yet available spatial resolution (1 μm^3) we had to increase the concentration of impurities significantly above the level found in most natural systems. Therefore, a direct comparison of our results to atmospheric hydrometeors is not possible, and is not the aim of this paper. We rather demonstrate that the presence of organics and inorganic impurities in a solution from which ice freezes has a profound effect on the sample morphology.

2 MATERIALS AND METHODS

2.1 Particle Sampling and Preparation

For all solutions high-purity MilliQ-water (resistivity 0.00055 μS) was used. The sodium bromide, quartz, bentonite, and octanol were of analytical grade (Sigma Aldrich). Emulsions of octanol with pure MilliQ-water or octanol with a 1 wt.% NaBr solution were prepared by filling a vial to one half with the organic solvent and to the other half with the aqueous solution. Suspensions were made from quartz and bentonite (clay) particles (size range 200 nm to 20 μm , 1 g mixed with 100 ml water) to simulate mineral dust components. The "mixed-mode-aerosol" suspensions were generated by adding the minerals or the octanol to the NaBr solution. All these formulations were shaken at 400 rpm for 24 hours prior to freezing in a vial with some head space. Thereby twofold equilibration was reached: The solutions were saturated with respect to both air and octanol.

After this step, fine droplets of these mixtures (0.2 μl) were placed on a hydrophobic paraffin substrate using a 10 μl syringe. Then this substrate was immediately exposed to 240 K in a refrigerator. After 24 hours in this environment, the frozen droplets were gently removed from the paraffin surface using a spatula that had been kept in the refrigerator all the time, and sealed airtight in plastic vials (Zinsser Analytics). All samples were prepared fewer than four days prior to the experiment and stored at 240 K. This temperature was a compromise in order to avoid a strong impact of shape metamorphism on the sample morphology^{24,25}. For practical matters, a preliminary comparison of a one-day-old with a four-days-old sample stored at these conditions, showed no changes in the shape of the sphere or distribution and morphology of the inclusions greater than the standard deviation of the geometrical characteristics of the structures measured in this study. Clearly, we cannot completely rule out the impact of shape metamorphism processes, which occur at a temperature of about 240 K. However, in this study we demonstrate the typical internal morphology of artificial samples frozen from a mixed solution. Therefore, metamorphism processes during sample storage are of minor significance for this study.

2.2 Cryotomography

A detailed description of the setup and data pretreatment was given previously²². In brief, the samples were transported on dry ice to the XTM end station MS-TOMO of the Swiss Light Source (SLS) at Paul-Scherrer-Institute at Villigen, Switzerland, where all experiments were conducted. Together with sample holders and the tools required for sample handling the samples were stored at all the times in a well isolated box, filled with dry ice. For every scan one ice particle (sample) was placed in a custom-made polyamide

cup adjustable to the standard sample mount at this beam line. This cup provided a maximum sample volume of 50 mm³. Ice particles were placed inside it, and the remaining space was filled with freshly molten cycloheptane (melting point approx. 260 K). The presence of the organic solvent mechanically fixes and thermally insulates the sample. The temperature was measured using a PT-100 resistor, which was placed at the bottom of the cup just a few tenth of a millimeter below the ice sample.

The experimental temperature was adjusted using a cold gas flow from a cryojet (Oxford Instruments) directed onto the head of the sample holder. The cup is surrounded by a double walled Kapton-foil cage. Dry nitrogen was flushed between the inner and the outer walls in order to avoid icing in the beam path while recording the tomogram.

For the transport from the dry ice box to the beam line, the sample holder was wrapped in a plastic bag filled with crushed dry ice. The Kapton-foil cage could be slid up onto the cryojet nozzle, which allowed easy access to the sample mount. The polyamide cup was placed into the sample mount, while being in the dry ice bag. Once fixed onto the goniometer stage, the dry ice bag was removed, and the Kapton-cage was slid down to ensure continuous cooling of the sample during final adjustments of the cup.

Then 500 projections were recorded during a 180 degree rotation of the sample holder. In order to correct for beam fluctuations, reference images were taken at every 100th angular step. The projections were used to reconstruct the 3D-image of the investigated object using an appropriate reconstruction algorithm^{26,27}. The camera allows a spatial resolution of 0.7 μm, but the data were immediately hardware-binned, which reduced the resolution to 1.4 μm, but improved the signal-to-noise ratio. The reconstructed slices were cropped to the desired region-of-interest (ROI), and, if necessary, filtered using a 2D edge-preserving smoothing filter (cf. detailed discussion by Miedaner et al.²⁰). The final image analysis was performed using the Amira software package (Mercury Systems).

2.3 Data analysis

The relative X-ray mass absorption of each component was coded as grey scale between 0 (strongest absorption in black) and 255 (lowest absorption in white) in the horizontal reconstructed slices. The segmentation was based on threshold values, whereby 0–10 was set for NaBr, 40–120 for ice, and 250–255 for air. Obvious reconstruction artefacts as well as segmented air bubbles inside the cycloheptane matrix were removed manually²². For data analysis, the number of pores, their individual volumes (V_i) and surface areas (A_i) were quantified. Connecting voids were identified using the numerical "burning algorithm" method²⁸. Additionally, we defined the deviation from the ideal spherical geometry as asphericity²⁹ Ψ_i :

$$\Psi_i = \frac{\pi^{\frac{1}{3}} (6V_i)^{\frac{2}{3}}}{A_i} \quad (1)$$

Furthermore, the volume-to-surface ratio was determined for each pore as it is common to characterize porous materials³⁰.

3 RESULTS

3.1 Octanol/H₂O Emulsion

Octanol, a common proxy for liquid organic urban aerosols³¹, could be clearly identified by the contrast change at the ice-octanol phase boundaries (cf. Figure 1). The very low contrast between air and octanol inclusions did not allow distinguishing between these two substances. This organic solvent occupied a total volume of $4.1 \cdot 10^{-7} \text{ m}^3$. The average

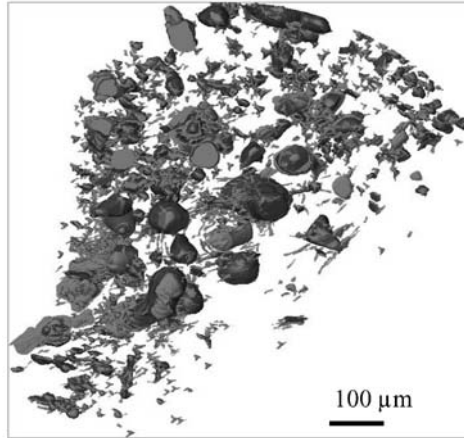


Figure 1 *Octanol inclusions in ice.*

surface area was found to be $2.5 \cdot 10^{-12} \text{m}^2$. The average asphericity reached a value of 0.59, while the volume-to-surface ratio was $2.7 \mu\text{m}$.

3.2 Octanol/H₂O/NaBr Emulsion

If a 1 wt.-% of NaBr was mixed with octanol prior to freezing, the shape of the resulting inclusions in the frozen sample changed significantly. The convex walls of the ice-octanol boundaries as observed in case of the pure solute, turned into concave ones (cf. Figure 2). The total surface area and total volume also increased significantly compared to solute samples without NaBr. The octanol/brine inclusions formed a very narrow and curly network throughout the whole sample, occupying an average surface area of $8.1 \cdot 10^{-9} \text{m}^2$ and an average volume of $2.2 \cdot 10^{-14} \text{m}^3$. The average asphericity increased to 0.63 compared to the pure octanol/H₂O system, while the volume-to-surface ratio decreased to an average value of $1.6 \mu\text{m}$.

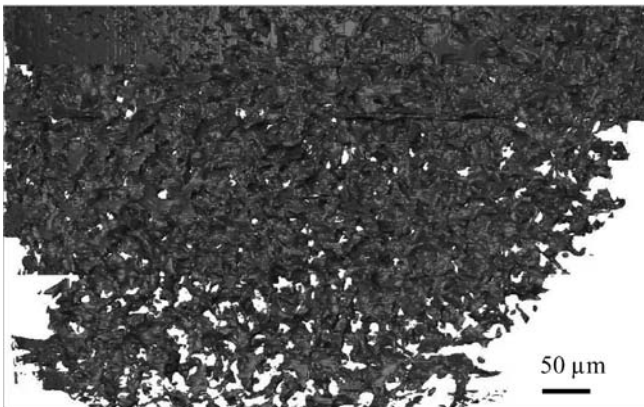


Figure 2 *NaBr/octanol inclusions in ice. Note the significant difference in shape compared to the inclusions of pure octanol depicted in Figure 1.*

3.3 Quartz Suspensions

Inclusions of quartz particles were found homogeneously distributed over the whole ice sample (cf. Figure 3). The average volume per inclusion was $4.4 \cdot 10^{-18} \text{m}^3$, while the average surface area reached a value of $5.7 \cdot 10^{-9} \text{m}^2$. The volume-to-surface ratio was found to be $0.77 \mu\text{m}$ with a mean asphericity of 0.36.

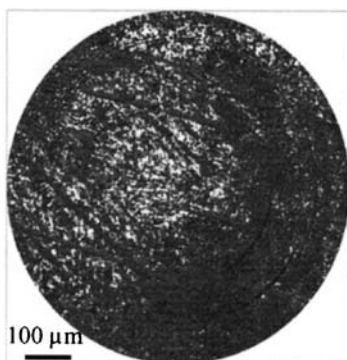


Figure 3 *Quartz particles in ice frozen from a quartz/MilliQ-water suspension.*

3.4 Quartz/NaBr Suspension

Freezing quartz particles suspended in a 1 wt.-% NaBr solution at a temperature of 240 K leads to small, homogeneously distributed inclusions in the ice (cf. Figure 4). An average inclusion volume of $6.0 \cdot 10^{-16} \text{m}^3$ with a surface area of $5.1 \cdot 10^{-10} \text{m}^2$ was found. The mean asphericity of these inclusions was 0.68, indicating that they have a rather spherical geometry. The volume-to-surface ratio also reached a low average value of $1.14 \mu\text{m}$. Since their asphericity and volume-to-surface ratio are significantly different from the inclusions in pure H_2O , a change in shape due to the addition of salt was observed.

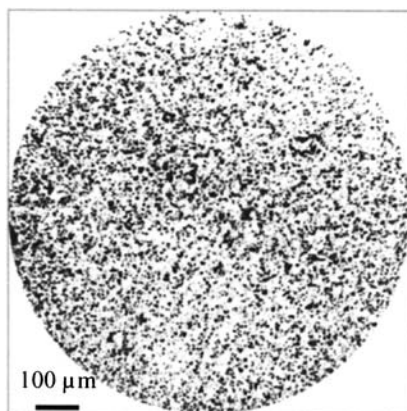


Figure 4 *Quartz inclusions in ice frozen from a NaBr-doped suspension.*

3.5. Bentonite

Figure 5 depicts the ice-trapped clay inclusions. The average impurity void filled a volume of $4.4 \cdot 10^{-13} \text{ m}^3$, with an average surface area of $1.3 \cdot 10^{-13} \text{ m}^2$. The mean volume-to-surface ratio was $0.36 \text{ } \mu\text{m}$. The clay particles were found to be agglomerated to elongated structures of a rather low asphericity of 0.25, much less than the above described quartz inclusions.

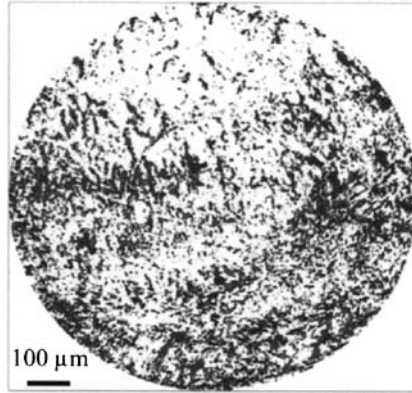


Figure 5 *Bentonite inclusions in ice frozen from a bentonite/MilliQ-water suspension.*

3.6 Bentonite/NaBr Suspension

Bentonite inclusions showed a completely different behavior upon freezing in a NaBr solution. Long, plate-like sheets almost perpendicular to each other were found (cf. Figure 6). An average surface area of $6.0 \cdot 10^{-9} \text{ m}^2$, and an average volume of $6.7 \cdot 10^{-15} \text{ m}^3$ were determined. The asphericity reached a mean value of 0.35, with a volume-to-surface ratio of $0.79 \text{ } \mu\text{m}$.

Similar to the quartz samples, asphericity and volume-to-surface ratio of the trapped inclusions changed upon addition of the salt - but more drastically in the case of bentonite.

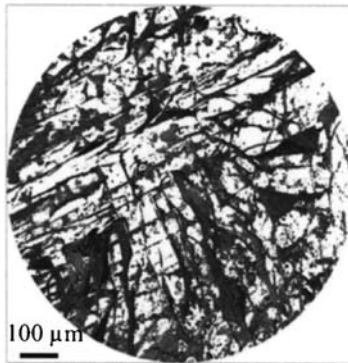


Figure 6 *Bentonite inclusions in ice frozen from a NaBr-doped suspension. Note the significant difference in shape compared to the bentonite particles in pure H₂O (cf. Figure 5).*

4 DISCUSSION

Quartz, bentonite, and octanol, as well as mixtures of these components with a 1 wt.-% NaBr solution, were frozen. The specific surface area, shape, and other geometric parameters were significantly different among the various samples studied. These differences depend on the chemistry of the impurity, as adding a salt to the solution or changing the mineral type had profound effects. In the case of freezing pure octanol/water emulsions, spherical inclusions of the octanol were found, which are caused by the strong hydrophobicity of octanol³¹. However, once an emulsion of a NaBr solution with octanol was made, the surface tension of the salt solution is higher compared to that of pure water^{31,32}, which obviously influences the shape and distribution of the octanol inclusions. The latter form a highly concave and well-connected network, if NaBr is present, but are convex if the salt is absent. Furthermore, air bubbles could not be identified, which suggests, that all the air could be dissolved in octanol. In addition, all NaBr-precipitates were found mixed into the octanol inclusions. The connectivity of this void network would allow for transport and further chemical reactions inside ice particles, and therefore may alter the chemical behaviour of such particles with respect to the surrounding gas phase as well as during contact with other solution droplets or changes in temperature.

Bentonite and quartz particles formed inclusions homogeneously distributed all over the sample, but of different shape. Both minerals showed a tendency towards agglomeration when they were mixed into a dilute salt solution. This is probably related to the difference in surface tension, which occurs due to the addition of the salt³². In particular, in the case of bentonite, one may speculate that also colloidal charging effects forced the inclusions to a more or less perpendicular orientation to each other inside the ice grain matrix. Additionally, the formation of pockets filled by highly concentrated brines occurs during freezing at low growth rates and significantly influences the morphology and distribution of the trapped inclusions³³, too.

5 SUMMARY AND CONCLUSIONS

Cryo-XMT was performed on various types of samples. For these experiments, a new setup was developed. It consists of a polyamide-cup, a cryojet, and a double-walled Kapton-foil-cage. By embedding the sample in cycloheptane inside the polyamide cup, the ice particles are not only fixed mechanically but also favorably isolated against temperature fluctuations. Experiments can be performed at temperatures as low as 230 K with an accuracy of ± 1 K and a stability of ± 3 K. To avoid icing in the path of the beam, all important parts are permanently flushed with dry gaseous nitrogen²². A spatial resolution of 1.4 μm was achieved in 1.75 hours per scan.

The systems studied in this work are not found in nature, where impurity concentrations are often lower. However, also in nature ice is frozen from aqueous solutions, leading to complex multiphase systems. The results presented here suggest there is an interdependence of all available impurities on the micro-morphology in the multiphase system. Such effects may have a profound impact on chemistry and transport of impurities, as such processes may occur just in the complex, three dimensional inclusions in the ice. It is beyond the scope of this paper to address these issues, but we believe that future applications of micro-tomography with much higher spatial resolution³⁴ will be well suited to further explore these issues.

Acknowledgements

Financial support for this research was provided by DFG via the SFB 641 (TROPEIS). A part of this work has been funded by the European integrated project SCOUT O3. This research project has been supported by the European Commission under the 6th Framework Program through the Key Action: Strengthening the European Research Area, Research Infrastructures n°: RII-CT-2004-506008. We are grateful to the PSI-SLS machine and beam line group whose outstanding efforts have made these experiments possible, in particular the practical support provided by the technicians M. Birrer, M. Lange, and D. Meister, and helpful discussions during the experiments by Dr. A. Groso.

References

- 1 J. Seinfeld and S. Pandis, *Atmospheric Chemistry and Physics*, 1997, Wiley Interscience.
- 2 G.M. Marion, *Geochim. Cosmochim. Acta*, 2002, **66**, 2499.
- 3 S. Solomon, *Nature*, 1990, **347**, 347.
- 4 P.J. Crutzen and F. Arnold, *Nature*, 1986, **324**, 651.
- 5 Th. Peter, *An. Phys. Chem.*, 1997, **48**, 785.
- 6 R.S. Gao, P.J. Popp, D.W. Fahey, T.P. Marcy, R.L. Herman, E.M. Weinstock, D.G. Baumgartner, T.J. Garrett, K.H. Rosenlof, T.L. Thompson, P.T. Bui, B.A. Ridley, S.C. Wofsky, O.B. Toon, M.A. Tolbert, B. Kärcher, Th. Peter, P.K. Hudson, A.J. Weinhiemer and A.J. Heymsfield, *Science*, 2004, **303**, 516.
- 7 K.S. Carslaw, T. Peter and S.L. Clegg, *Rev. Geophys.*, 1997, **35** (2), 125.
- 8 S.L. Clegg and J.H. Seinfeld, *J. Phys. Chem. A*, 2006, **110** (17): 5692.
- 9 A.W. Rempel and J.S. Wettlaufer, *J. Geophys. Res.*, 2002, **107**, B12, 2330.
- 10 A. Carte, *Proc. Phys. Soc.*, 1961, **77**, 757.
- 11 L. Keyser and M. Leu, *Microsc. Res. Tech.*, 1993, **25**, 434.
- 12 P. Barnes, R. Mulvaney, E. Wolff and K. Robinson, *J. Microsc.*, 2002, **205**, 118.
- 13 P. Barnes, E. Wolff and D. Mallard, *Mic. Res. Tech.*, 2003, **62**, 62.
- 14 D. Cullen and I. Baker, *Mic. Res. Tec.*, 2001, **55**, 198.
- 15 R. Mulvany, E. Wolff and K. Oates, *Nature*, 1988, **331**, 247.
- 16 H. Fukazawa, K. Sugiyama and S. Mae, *J. Phys. Chem.*, 1997, **101**, 6184.
- 17 H. Ohono, M. Igarashib and T. Hondoha, *Earth, Planet. Sci. Lett.*, 2005, **232** (3), 171.
- 18 M. Schneebeli and A. Sokratov, *Hydr. Proc.*, 2004, **18**, 3655.
- 19 J.B. Brzoska, C. Coleou, B. Lesaffre, S. Borel, O. Brissaud, W. Ludwig, E. Boller and J. Baruchel, *ESRF Newsletter*, 1999, 22.
- 20 Flin, F., J.B. Brzoska, B. Lesaffre, C. Coleou and R.A. Pieritz, *J. Phys. D.: Appl. Phys.*, 2003, **36**, A49.
- 21 Flin, F., J.B. Brzoska, B. Lesaffre, C. Coleou and R.A. Pieritz, *Ann. Glaciol.*, 2004, **38**, 39.
- 22 M. Miedaner, T. Huthwelker, F. Enzmann, M. Kersten, M. Stampanoni and M. Amman, submitted
- 24 A. Cabanes, L. Legagneux and F. Domine, *Env. Sci. Tech.*, 2003, **37**, 4, 661.
- 25 S.C. Colbeck, *J. Appl. Phys.*, 1983, **54**, 2677.
- 26 G. Herman, *Image reconstruction from projections*, 1980, Academic Press.
- 27 J. Radon, Ber. Verb. Saechs. Akad. Wiss., Leipzig, *Math. Phys. Kl.*, 1917, **69**, 262.
- 28 D. Stauffer and A. Aharony, *Introduction to Percolation Theory*, Taylor & Francis, London, 1992.
- 29 H. Wadell, *J. Geol.*, 1933, **41**, 310
- 30 S. Brunauer, R. Mikhail and E. Bodor, *J. Coll. Interf. Sci.*, 1967, **24**, 451.
- 31 Y. Rudich, *Chem. Rev.*, 2003, **103**, 5097.

- 32 M. Boström, D.R.M. Williams and B.W. Ninham, *Langmuir*, 2001, **17**, 4475.
- 33 M.G. Worster and J.S. Wettlaufer, *J. Phys. Chem. B*, 1997, **101**, 6132.
- 34 D. Attwood, *Nature*, 2006, **442**, 642.

